

## ON THE ABILITY OF CONVENTIONAL AERODYNAMIC PROBES TO RESOLVE HIGH FREQUENCY PHENOMENA

Zhe Liu  
Purdue University  
Indiana, United States

Guillermo Paniagua  
Purdue University  
Indiana, United States

### ABSTRACT

This paper investigates numerically an oval and trapezoidal probe from the steady and unsteady point of view, in a wide range of Mach 0.3 and 0.75 at several yaw angles. Angular sensitivity as well as static / total pressure distortion was determined. The sensitivity to probe induced unsteady vortex shedding was computed during steady operation as well as during transients. The dynamic response of the pressure tapings were carefully analyzed performing unsteady Reynolds Averaged Navier Stokes (URANS) simulations. The dynamic response of pressure tapings indicates that vortex shedding unsteadiness propagates into the sensors.

### NOMENCLATURE

Symbol	
$a$	Sonic speed[m/s]
$CCF$	Cross-correlation coefficient
$C_p$	Pressure coefficient
$D$	Probe diameter[mm]
$D_t$	Tube diameter[mm]
$f_n$	Resonance frequency[kHz]
$f_A$	Fuzzy set for DFT amplitude convergence
$f_\phi$	Fuzzy set for DFT phase convergence
$f_M$	Fuzzy set for time-mean convergence
$f_s$	Fuzzy set for convergence of signal shape
$f_c$	Fuzzy set for overall convergence
$f$	Vortex shedding frequency[kHz]
$f_n$	Resonance Frequency[kHz]
$L$	Tube length[mm]
$M$	Mach number
$MinMax$	Maximum-minimum
$i$	Points on the curvilinear coordinate
$Ps_i$	Measured static pressure[Bar]
$P_s$	Inlet static pressure[Bar]
$P_{sensor}$	Static pressure measured by sensor
$P_t$	Inlet total pressure[Bar]
$Re$	Reynolds number
$s$	Curvilinear coordinate
$St$	Strouhal number
$U$	Free stream velocity [m/s]
$V_c$	Cavity Volume[m <sup>3</sup> ]
$V_t$	Tube Volume[m <sup>3</sup> ]

### INTRODUCTION

Aerodynamic probes are ubiquitous in turbomachinery research and gas turbine monitoring. The wide variety of multi-hole probes can be classified according to their shape [1]. Dominy and Hodson [2] evaluated the effect of different five-hole probe geometries on the size and location of the recirculation bubble. Villafane et al [3] measured in their lab the angle sensitivity of conical and oval probes and errors on the angle determination during the experimental calibration. To improve the accuracy in transonic measurements, Kost [4] proposed the use of an additional pressure tapping in the base region. Regrettably the previously described experimental procedures is not suitable for the optimization of the ideal probe for a transonic application. Calibrated numerical tools offer an alternative procedure to yield insights into the detailed aerodynamics within the probe, and the ability to couple with optimizers.

In this paper, numerical analysis is performed on the angle sensitivity and induced unsteadiness sensitivity of the oval and trapezoidal probes, hemispherical and conical respectively in 3D. The studies were performed over a wide range of Mach numbers from subsonic to the transonic regime, using a 2D URANS solver. The vortex shedding affects noticeably the pressure readings. Resonance frequency of tube-cavity system was evaluated performing transient simulations.

### METHODOLOGY

This numerical investigation consisted on two different steps. First we characterized two different probe geometries, and their performance at different incidence angles, regarding pressure coefficients as well as the propagation of the vortex shedding effects upstream. In the second evaluation we selected the oval probe geometry, but now including the line-cavity effects into the pressure tapings.

Fig.1 shows the two investigated probe geometries, both with identical overall dimensions, i.e.  $4.4 \times 2.2 \text{ mm}^2$ . The computational domain is  $100 \times 100 \text{ mm}^2$ , covering more than 20 times the probe dimension upstream and downstream. The

grid was unstructured, with 259407 cells. The  $y^+$  was lower than 1 in all the simulations.

The URANS solver is ANSYS Fluent 16.2, density based solver. The turbulence closure was provide with the K- $\omega$  SST model, which is well suited for adverse pressure gradients and separated flows. The analysis was performed at several Mach numbers, but here we report the results at Mach 0.3, 0.6 and 0.75. For the unsteady subsonic calculations, we selected a time step of  $1\mu s$ , whereas for the transonic regime the time step is  $0.1\mu s$ . The data was stored every  $10\mu s$ , allowing to resolve a maximum frequency of 100 kHz. The observation window in all frequency analysis was 2ms to ensure 0.5kHz frequency resolution. The total computational time for each simulation was about 576 hours on an Intel(R) Xeon(R) CPU 2.40Ghz machine.

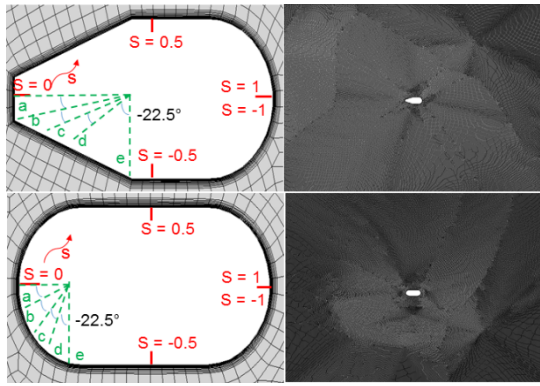


Figure 1: Top) Trapezoidal probe geometry and computational domain. Bottom) Oval probe geometry and computational domain

The curvilinear coordinate “ $S$ ” shown in Fig.1 is defined around the probe perimeter. To quantify the angle sensitivity, we use the pressure coefficient which is the local static pressure at the location “ $i$ ” compared to the undisturbed flow static pressure, non dimensionalized by the dynamic pressure:

$$C_{pi} = \frac{P_{si} - P_s}{P_t - P_s} \quad (1)$$

In the equation  $P_t$  and  $P_s$  are the undisturbed flow total and static pressures, imposed far upstream, at the inlet of the computational domain.

Statistical analyses were performed at five equiangular positions along the curvilinear coordinates: “a”, “b”, “c”, “d”, “e”. The flow field around the probe is intrinsically unsteady, primarily due to the instantaneous vortex shedding. Hence, the flow properties periodically oscillate instead of converging to fixed values. We selected location “a”, at the leading edge, to assess the convergence.

Fig. 2-top shows the pressure signal at the probe leading edge. Fig. 2-center displays a zoomed portion of the previous trace, comprising seven consecutive periods. In Fig. 2-bottom the three last periods agree very well with each other.

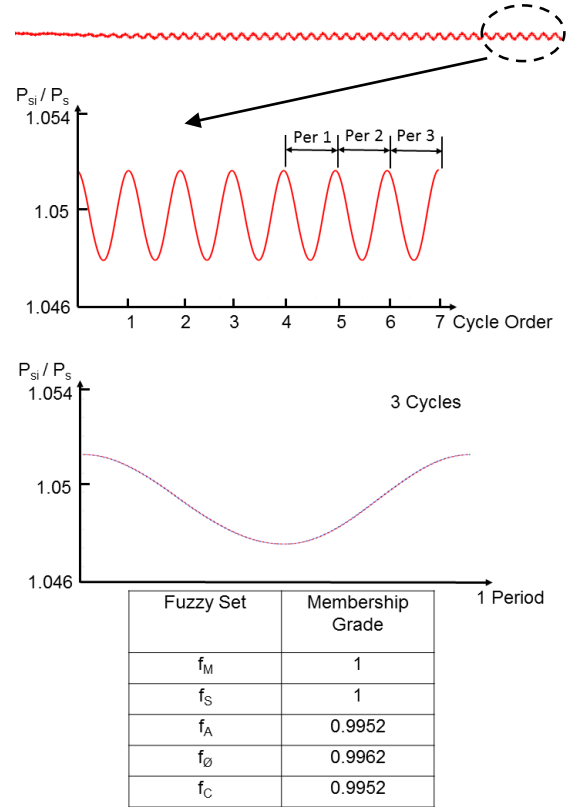


Figure 2: Periodic unsteady convergence

To assess convergence we use the method of Clark and Grover [5], by generating a series of fuzzy set, mean-level fluctuations during the numerical evaluation. Discrete Fourier Transform (DFT) amplitudes and phases at frequency of interest, and cross-correlation coefficients at each periodic cycle are performed. Two consecutive cycles form a pair and are compared to calculate the membership grade of period convergence in each fuzzy sets. In this case, 6 pairs need to be computed. An overall fuzzy set is then formed by using multi-valued logic to describe the overall periodic convergence, refer to Klir and Yuan [6] for detailed fuzzy set theory. Equations (2) to (7) are applied to calculate each fuzzy set.

$$CCF(P_1, P_2) = \frac{\sum_{n=1}^N P_1 P_2}{[\sum_{n=1}^N P_1^2 \sum_{n=1}^N P_2^2]^{\frac{1}{2}}} \quad (2)$$

$$f_M = 1 - \left| 1 - \frac{\bar{P}_{current}}{\bar{P}_{previous}} \right| \quad (3)$$

$$f_A = 1 - \left| 1 - \frac{A_2}{A_1} \right| \quad (4)$$

$$f_\phi = 1 - \left| \frac{\phi_2 - \phi_1}{\pi} \right| \quad (5)$$

$$f_S = CCF(P_1, P_2) \quad (6)$$

$$f_C = \min(f_M, f_A, f_\phi, f_S) \quad (7)$$

where  $P_1$  and  $P_2$  represent non-dimensional static pressure of previous cycle and current cycle. The frequency of interest in this case is vortex shedding frequency, therefore DFT fuzzy set analysis is performed at vortex shedding frequency. Membership grade of each fuzzy set is shown in Fig.2. When  $f_c \geq 0.95$  is achieved for two consecutive cycles periodic convergence achieved.

**PROBE SHAPE CHARACTERIZATION AT SEVERAL INCIDENCE ANGLES**

Fig 3 displays the steady Mach contour with yaw variation in subsonic flow. Fig.4 shows static pressure non-dimensionalized by the undisturbed flow static pressure. A contour of pressure coefficient at a, b, c, d, and e at various yaw is depicted in Fig.5 combined with the magnitude of pressure coefficient difference  $C_p(\text{large yaw}) - C_p(0 \text{ yaw})$  at point a and c.

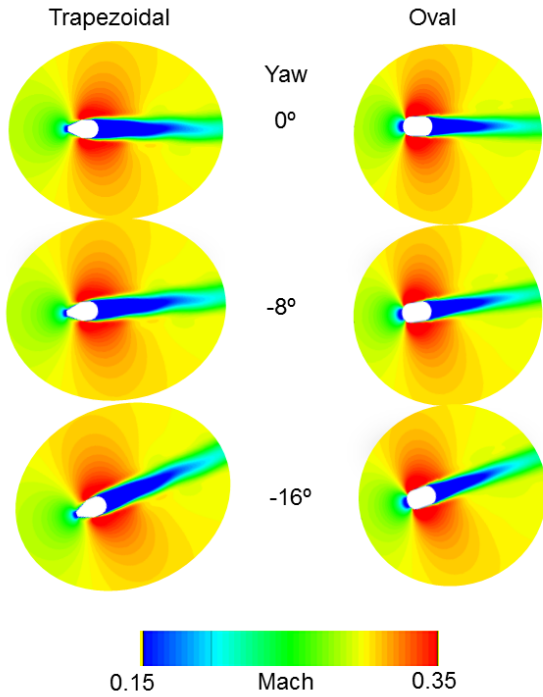


Figure 3: Steady Mach contour when Mach=0.3

Fig.5-top shows that static pressure changes with yaw variation and total pressure was recovered at 0 yaw. More total pressure was recovered on the lateral tappings (b,c) of the oval probe than on the trapezoidal probe. Fig.5-bottom indicates that both the trapezoidal and oval show almost the same angle sensitivity at smaller yaw at the center tapping. However, as yaw increases, oval is more sensitive to yaw variation. Fig.5-bottom displays that the trapezoidal cone shows higher angle sensitivity on the lateral tapping c.

When undisturbed flowfield approached transonic, Fig.8-top displays a smaller total pressure

recoveries on the lateral tappings (c,d,and e) of the trapezoidal probe compared with the oval probe. Comparison between Fig. 8-bottom and Fig.5-bottom indicates that angle sensitivity of both shapes was decreased when flowfield approached transonic. At the lateral tapping 'c', the angle sensitivity advantage of the trapezoidal probe was even reversed when yaw became larger.

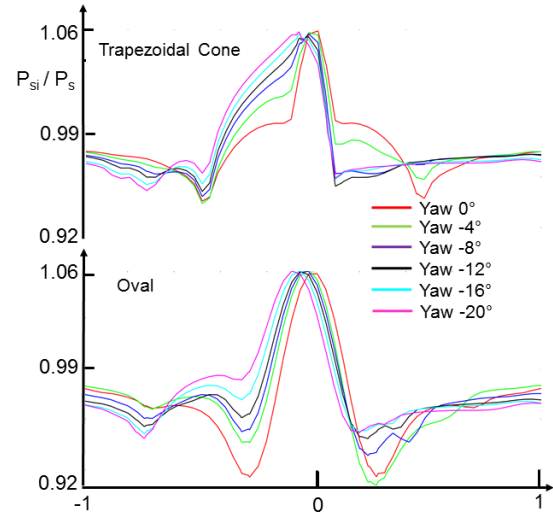


Figure 4: Non-dimensional static pressure as a function of curvilinear coordinates and yaw when Mach=0.3

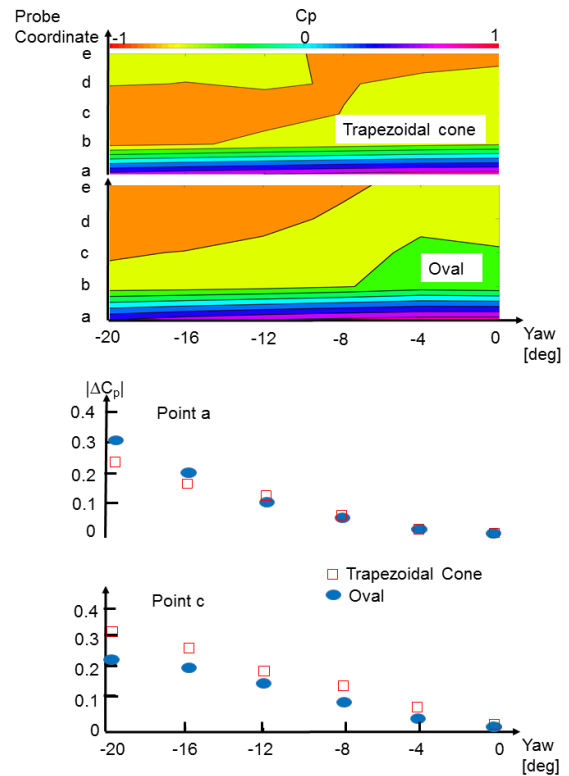


Figure 5: Iso-contour of  $C_p$  as a function of yaw and coordinates (a,b,c,d,e) along probe nose and magnitude of pressure coefficient difference between 0 and different yaw at point a,c when Mach=0.3

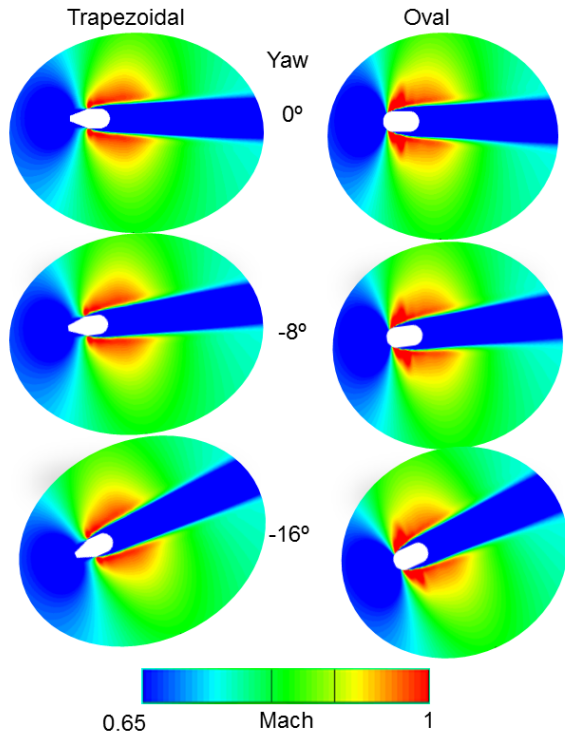


Figure 6: Steady Mach contour when Mach=0.75

The sensitivity to induced vortex shedding unsteadiness was evaluated when selecting locations of the lateral pressure tappings. Fig.9 and Fig.10 shows respectively the instantaneous vortex shedding downstream of the two probes at 0 yaw in Mach=0.3 and Mach=0.75. Vortex shedding frequencies based on URANS simulations are detailed in Table 1, together with results from St-Re correlation for confined flow [7] which were evaluated applying Eq.8. Results show a higher vortex shedding frequency obtained from the oval probe, which indicates an enhanced unsteadiness propagation.

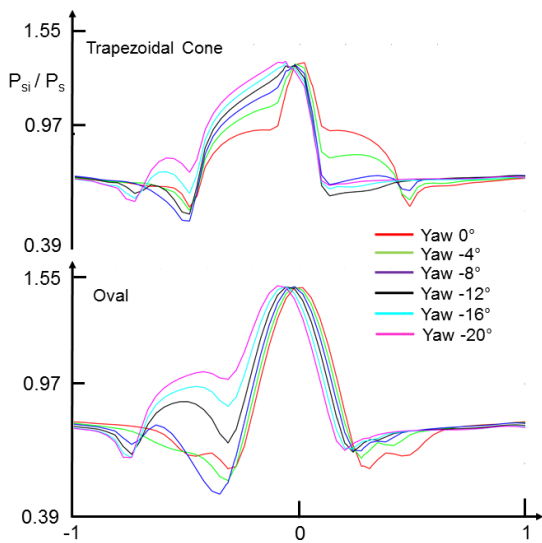


Figure 7: Non-dimensional static pressure as a function of curvilinear coordinates and yaw when Mach=0.75

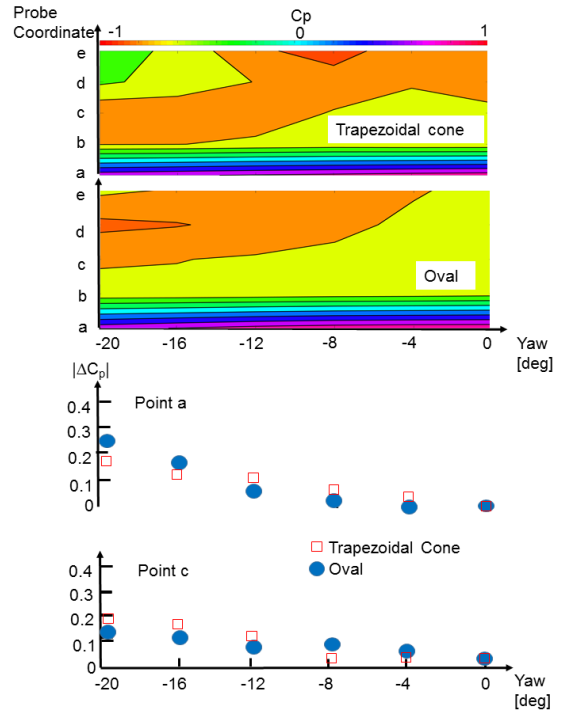


Figure 8: Iso-contour of  $C_p$  as a function of yaw and coordinates (a,b,c,d,e) along probe nose and magnitude of pressure coefficient difference between 0 and different yaw at point a,c when Mach=0.75

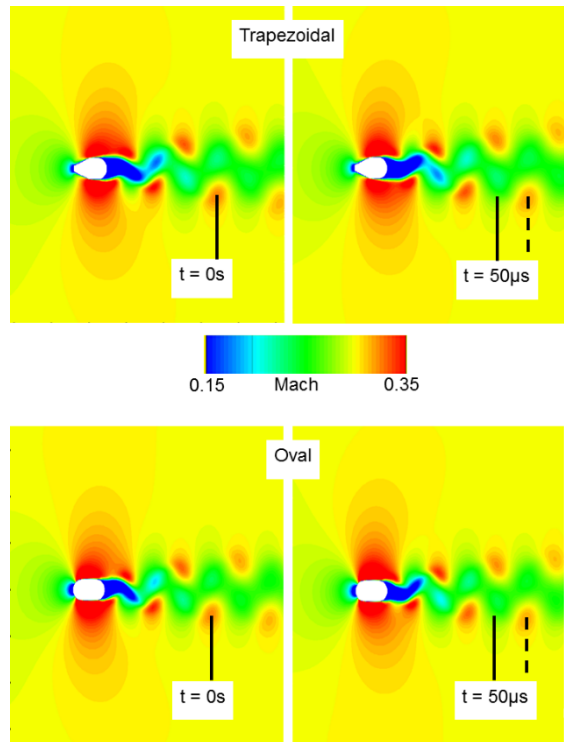


Figure 9: Vortex shedding downstream of the probe at Mach=0.3 and 0 yaw

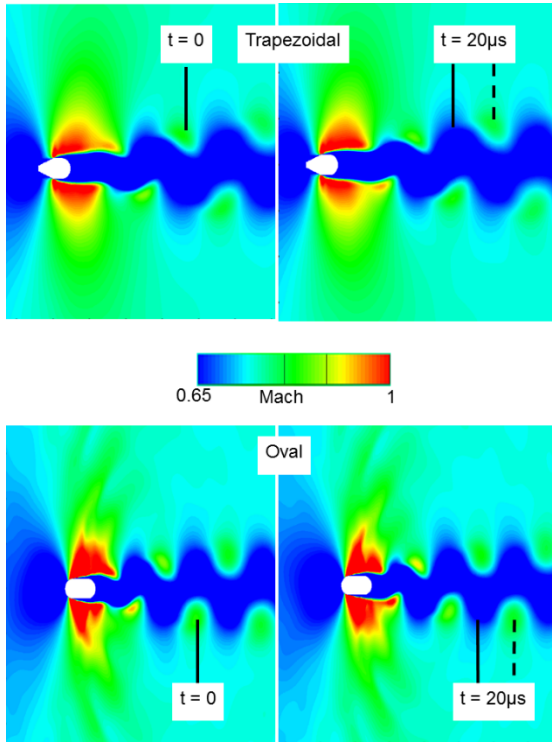


Figure 10: Vortex shedding downstream of the probe at Mach=0.75 and 0 yaw

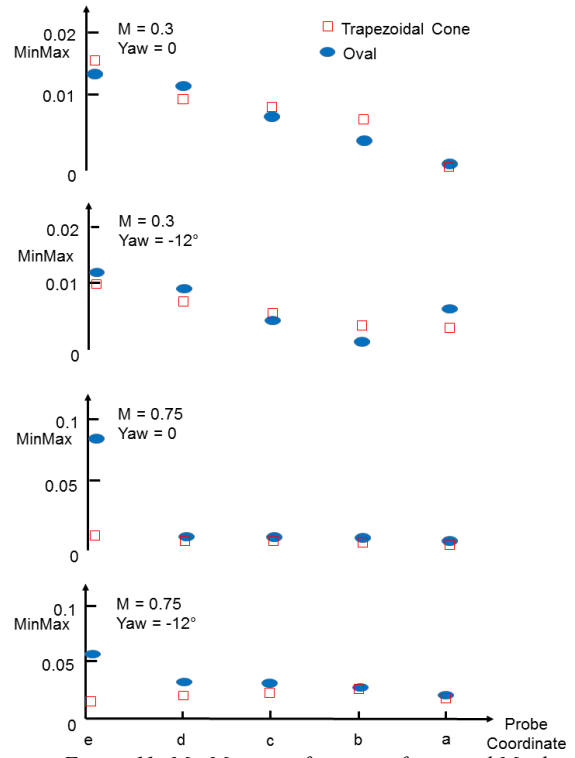


Figure 11: MinMax as a function of yaw and Mach

	Mach=0.3		Mach=0.75	
	Trapezoidal	Oval	Trapezoidal	Oval
CFD Calculation	10.7±0.5kHz	11.3±0.5kHz	18.6±0.5kHz	21.8±0.5kHz
Strouhal Reynolds Correlation	9.0~9.2kHz		19.8~20.3kHz	
	22800	22800	46300	46100
	Re		Re	

Table 1: Strouhal-Reynolds correlation

$$St = \frac{fD}{U} \quad (8)$$

Where  $f$  is vortex shedding frequency,  $D$  is probe diameter and  $U$  is free stream velocity.

Statistical analysis is implemented to investigate unsteadiness sensitivity and results are depicted in Fig.11. Fig.11-top shows that the oval probe is less affected by the unsteadiness at 0 yaw. When flowfield approached transonic, bottom two figures imply that the vortex shedding unsteadiness was increased due to the higher vortex shedding frequency and lateral tapping 'c' should be avoid on the oval probe where induced unsteadiness is severely strong.

### OVAL PROBE WITH PRESSURE TAPPINGS

The oval probe is shown in Fig.23. One central and two lateral tappings are drilled perpendicular to head surface. The angular positions between central and lateral tappings are located at  $\pm 50^\circ$ . The diameter of line is 0.3mm and the diameter of cavity is 0.6mm.

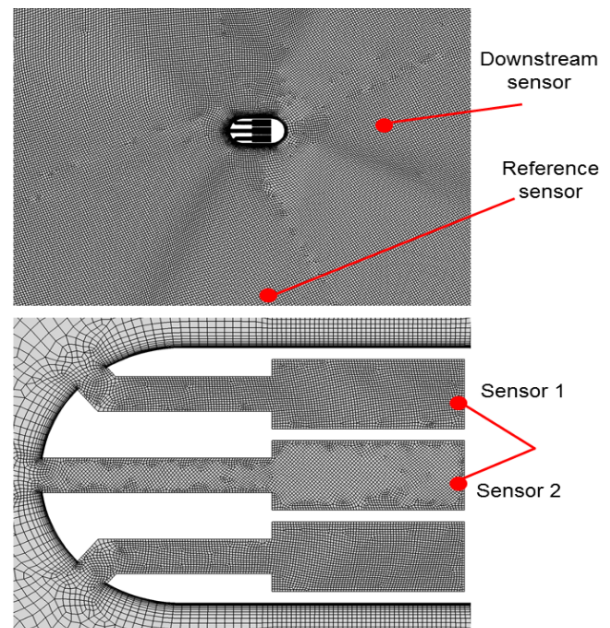


Figure 12: Oval probe

The analysis of the unsteady circulation, and effect of the pneumatic line is fundamental to ensure

an accurate pressure reading. Instantaneous pictures of the vortex shedding downstream of the probe at Mach=0.3 and Mach=0.6 are shown in Fig.14. Frequency analyses were performed on the downstream flow velocity non-dimensionalized by undisturbed flow velocity  $U_{\text{sensor}}/U$  as well as measured pressure signal non-dimensionalized with undisturbed flow static pressure  $P_{\text{sensor}}/P_s$  in the Sensor 1 and 2 to retrieve vortex shedding frequency and the dynamic response of the pressure tappings.

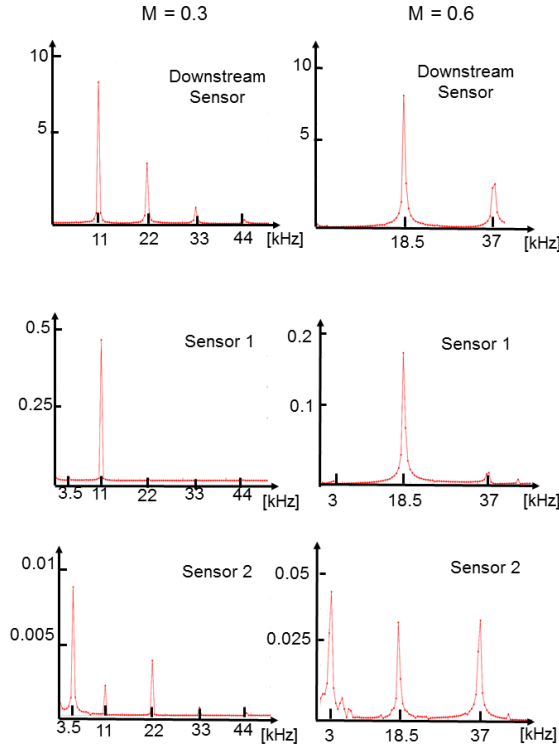


Figure 13: Unsteadiness propagation of vortex shedding into the oval probe

Fig.13 top identifies the vortex shedding frequency is  $11 \pm 0.5$  kHz at Mach=0.3 and  $18.5 \pm 0.5$  kHz at Mach=0.6. Interestingly, at Mach=0.3, Fig.13-top-left reveals the first, the second, and the third harmonic after the dominant vortex shedding frequency and their amplitude is decreasing by half. At Mach=0.6, Fig. 13 top-right reveals the second harmonic occurs and its amplitude decreases by half.

Frequency response of pressure tappings at sensor 1 reveals the same dominant vortex shedding frequency. The amplitude of the harmonic is far lower than the dominant frequency especially at lateral pressure tapping. However, in the sensor 2, response is dominated by the moving acoustic wave which is  $3.5 \pm 0.5$  kHz. This was verified by the fact that the sound speed at sensor 2 was 336.2 m/s and the length of the computational domain is 100 mm, therefore analytic frequency of the moving acoustic wave is 3.36 kHz. Fig.13 implies that induced vortex shedding unsteadiness has propagated into pressure tappings where sensors are located

Similarly, at Mach=0.6, shedding unsteadiness has also propagated into pressure tappings. However, frequency of the moving acoustic wave is attenuated to 3 kHz due to the increased speed of flowfield which increase of the speed of the reflected acoustic wave.

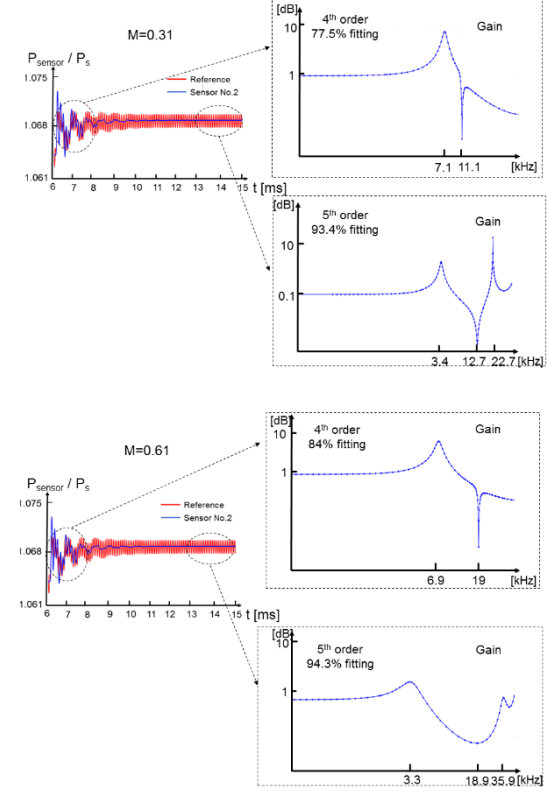


Figure 14: Transfer function identification

Helmholtz theory is implemented to predict resonance frequency of central tube-cavity system where sensor 2 located. The theory is expressed as:

$$f_n = \frac{a}{2\pi} \sqrt{\frac{\pi D_t^2}{4LV_c}} \quad (9)$$

Where  $a$  is sonic speed,  $D_t$  is tube diameter,  $L$  is tube length, and  $V_c$  is the volume of the cavity. Helmholtz theory predicts 16.3 kHz. Helmholtz theory works better when the cavity length is negligible compared with the line length [8]. For the oval probe, it is obviously not applicable. Hougen et al [9] introduced a more accurate model which considering compressible flow effects in the line defined as:

$$f_n = \frac{a}{2\pi L} \sqrt{\frac{1}{0.5 + \frac{V_c}{V_t}}} \quad (10)$$

Where  $V_t$  is tube volume. The modified resonance frequency of the center cavity is 15.2 kHz. In order to validate the analytic model applied, after

the unsteady simulations are periodically converged at  $t=6\text{ms}$ , a total pressure step was initiated at pressure inlet. Reference sensor is 18D downwards from sensor 2 shown in Fig.12. The obtained transfer functions are shown in Fig.14. The cavity resonance frequency from numerical approach is identified as 7.1 kHz at Mach=0.3 and 6.9 kHz at Mach=0.6 which are less than 50% of the theoretical value, implying the overestimation of the analytic model on predicting the resonance frequency of the tube-cavity system.

## CONCLUSION

Steady results show that total pressure recovery is higher on the lateral tappings of the oval probe. Trapezoidal probe shows higher angle sensitivity on the lateral tappings in subsonic flow. However, transonic effect decreases angle sensitivity of both shapes and this is more serious on the trapezoidal probe. Unsteady sensitivity is enhanced due to the higher vortex shedding frequency when flowfield approached transonic. Frequency analysis reveals the induced unsteadiness propagated into the pressure tappings. Interestingly, the present numerical results shows values, about half of what we would expect from the traditional analytical models.

## REFERENCES

- [1] Bryer, D.W., and Pankhurst, R.C., 1971, "Pressure probe methods for determining wind speed and flow direction," Her Majesty's Stationary Office, p. 125.
- [2] Dominy, R.G., and Hodson, H.P., 1993, "An investigation of factors influencing the calibration of 5-hole cone and pyramid probes," ASME Journal of Turbomachinery, 115: 513-9.
- [3] Villafane L., Yasa T., Paniagua G., Bonfanti G., 2011, "Development of Experimental Techniques for the Characterization of Helicoidal Fin Arrays in Transonic Flow Conditions". *Proceedings of the 47<sup>th</sup> AIAA/ASME/SAE/ASEE Joint Propulsion Conference*. AIAA-2011-6093. DOI: 10.2514/6.2011-6093. eISBN: 978-1-60086-949-5. San Diego, USA. July.
- [4] Kost F., "Probes in transonic flow," XIX Biannual symposium on measuring techniques in Turbomachinery, Transonic and Supersonic Flow in Cascades and Turbomachines, April 7-8, 2008, Rhode-St-Genèse, Belgium.
- [5] Clark, J.P., and Grover, E.A., 2006, "Assessing convergence in predictions of periodic-unsteady flowfields," ASME Journal of Turbomachinery, 129(4), 740-749.
- [6] Klir, G.J., and Yuan, B., 1995, "Fuzzy Sets and Fuzzy Logic: Theory and Applications," Prentice Hall PTR, Upper Saddle River, NJ.
- [7] Richter, A., and Naudascher, E., 1976, "Fluctuating forces on a rigid circular cylinder in confined flow," J. Fluid Mech, vol. 78, part 3, pp. 561-576.
- [8] Persico, G., Gaetani, P., and Guardone, A., 2005, "Design and analysis of new concept fast-response pressure probes," Measurement Science and Technology, vol. 16, pp. 1741-1750.
- [9] Hougen, J.O., and Martin, O.R., 1963, "Dynamics of pneumatic transmission lines," Control Eng., Vol. 10, pp 114-7.